Time-Dependent Algorithms for Viscoelastic Flow - finite element/volume schemes

M. F. Webster
Institute of Non-Newtonian Fluid Mechanics
Department of Computer Science
University of Wales, Swansea
Singleton Park, Swansea SA2 8PP, U.K.

H. R. Tamaddon-Jahromi M. Aboubacar

Hybrid finite volume/element methods are investigated within the context of transient viscoelastic flows. A finite volume algorithm is proposed for the hyperbolic constitutive equation, of Oldroyd-form, whilst the continuity/momentum balance is accommodated through a Taylor-Galerkin finite element method. Various finite volume combinations are considered to derive accurate and stable implementations. Consistency of formulation is key, embracing fluctuation distribution and median-dual-cell constructs, within a cell-vertex discretisation on triangles. In addition, we investigate the effect of treating the time-term in a finite element fashion, using mass-matrix iteration instead of the standard finite volume mass-lumping approach. We devise an accurate transient scheme that captures the analytical solution at short and long time, both in core flow and near shear boundaries. In this respect, some difficulties are highlighted. A new method emerges, with the Low Diffusion B (LDB, with or without mass-matrix iteration) as the optimal choice. We progress to a complex flow application and demonstrate some provocative features due to the influence of true transient boundary conditions on evolutionary flow-structure in a 4:1 start-up rounded-corner contraction problem.

Keywords: Hybrid finite volume; flux and source distribution schemes; time-dependent; accuracy; stability; viscoelasticity

Numerical Methods for Partial Differential Equations (Volume Number), 1?? ((Year))

I. INTRODUCTION AND GOVERNING EQUATIONS

In previous studies [1, 2, 3], we devised stable and accurate steady-state hybrid finite volume/finite element algorithms to simulate complex viscoelastic flows. These schemes were applied successfully to flow past cylinder [1], and to the benchmark flow of an Oldroyd-B fluid through a planar sharp 4:1 contraction [2]. Subsequently, application was extended to various Phan-Thien/Tanner model fluids, contrasting planar and axisymmetric flows through sharp and rounded-corner contractions [3, 4]. Such advances were achieved by ensuring consistency in the treatment of flux and complex source-terms (solution and velocity-gradient dependent), which arise in the constitutive equation. Now, as a consequence, transients may be seriously addressed and time-accuracy delivered.

We have undertaken such a task in two distinct phases. First, through spatial discretisation adjustments (viewed as right-hand-side stress equation terms). Secondly, through consideration of time-term approximations (left-hand-side terms). Hence, under the spatial phase, we outline a series of variants under "Fluctuation Distribution", (FD), both with and without Median-Dual-Cell (MDC) contributions. This leads to recommendations as to optimal selection of upwinding factors (α_l^T) of FD-schemes. Subsequently, we turn to the blending of fluctuation distribution and Median-Dual-Cell contributions to the temporal stress-residual.

Lastly, we identify the link between finite volume (fv) and finite element (fe) spatial contributions. This simply recognises the fact that at the fv-cell level, the sum of the linear Galerkin interpolant contributions naturally yields the amalgamated finite volume residual to that cell. The second phase of study addresses the discrete approximation of the fv time-term, $\int_{\Omega_T} \frac{\partial \tau}{\partial t} d\Omega_T$. Here, again we identify the link to Galerkin discretisation (fe), and place this alongside a standardised iteration, based around a consistent Mass-matrix formulation. The success of this approach may be judged critically against the attainment of minimal error in stress and velocity, both in amplitude and phase as a function of time, measured from the theoretical position.

Justification, in broad terms, for the use of such hybrid schemes may be found in their ability to achieve high-order accuracy, whilst retaining stability and when applied judiciously, both in the transient as well as at steady-state. They are responsive and appropriate for use in combination with unstructured meshing (an advantage over spectral schemes). Hence, they find application equally on complex smooth and non-smooth viscoelastic problems, as we proceed to demonstrate. The numerical deliberation above are taken first against a model transient viscoelastic flow problem, start-up Poiseuille channel flows for an Oldroyd-B fluid, leading on to a complex flow, that of transient viscoelastic flow through a contraction. The literature in this area was covered in Matallah et al. [5]. In this regard, one notes the work of Sato and Richardson [6], utilising a hybrid finite element/finite volume method with a pressure-correction scheme and a time-stepping procedure. Their results documented the transient evolution in velocity (alone) for planar channel Poiseuille flow, and pseudo-transient solutions (via streamlines, and progressively We-increasing states) for a 4:1 planar sharp-corner contraction. Similarly, transient solutions were reported by Olsson [7] for a Giesekus fluid and a rounded-corner contraction geometry, using a method-of-lines time integration procedure and a finite-difference spatial discretisation. In addition, the same start-up channel Poiseuille-flow for an Oldroyd-B fluid was considered more recently by Fiéter and Deville [8], to expose the properties of spectral element methods in this regime. This work, as

our own, enforced analytical transient inlet boundary conditions on velocity and stress, following Waters and King [9]. These authors noted that accuracy in the transient revealed typical errors of the order of a few percent, reflecting our own findings likewise. In the present article, we go further and consider complex flows, where in particular we analyse the influence of dynamic boundary conditions on evolutionary flow-structure for start-up flow of Oldroyd-B fluids in a 4:1 rounded-corner contraction. In this respect, we point to the conspicuous trends through the transient states in vortex activity and stress fields. We are able to comment upon our transient findings, in contrast to those of others in this context, who largely have appealed to fixed-point steady-state driving boundary conditions, on the basis of far-field assumptions. We demonstrate the outcome when such assumptions are avoided.

Incompressible viscoelastic flows are governed by conservation laws for mass and momentum, and a constitutive equation for stress. In non-dimensional form, the balance equations under isothermal conditions may be represented as:

$$\nabla \cdot \boldsymbol{u} = 0, \tag{1.1}$$

$$Re\frac{\partial \boldsymbol{u}}{\partial t} = -Re\,\boldsymbol{u}\cdot\nabla\boldsymbol{u} - \nabla p + \nabla\cdot\left(2\frac{\mu_2}{\mu}\boldsymbol{d} + \boldsymbol{\tau}\right). \tag{1.2}$$

Utilising the Oldroyd-B constitutive equation for the equation of state, the stress $\boldsymbol{\tau}$ is given by:

$$We\frac{\partial \boldsymbol{\tau}}{\partial t} = -We\,\boldsymbol{u}\cdot\nabla\boldsymbol{\tau} + 2\frac{\mu_1}{\mu}\boldsymbol{d} + We\,(\boldsymbol{L}\cdot\boldsymbol{\tau} + \boldsymbol{\tau}\cdot\boldsymbol{L}^T) - \boldsymbol{\tau}. \tag{1.3}$$

Here, $\boldsymbol{u}$, p, $\boldsymbol{\tau}$ represent the fluid velocity, the hydrodynamic pressure and the extra-stress tensor; $\boldsymbol{d} = (\boldsymbol{L}+\boldsymbol{L}^T)/2$ represents the Eulerian rate-of-deformation tensor and $\boldsymbol{L}^T = \nabla\boldsymbol{u}$, the velocity gradient. The total viscosity μ is split into Newtonian solvent (μ_2) and polymeric (μ_1) contributions, such that $\mu = \mu_1 + \mu_2$. The Oldroyd-B model is a constant shear viscosity model fluid (with an unbounded elongational viscosity at finite strain rates).

Non-dimensional group numbers are Reynolds ($Re = \frac{\rho UL}{\mu}$) and Weissenberg ($We = \frac{\lambda U}{L}$) numbers, defined with reference to material parameters ρ, λ of fluid density and relaxation time, and U, L, characteristic velocity and length scales for the flow. Creeping flow for $4:1$ contraction problem is represented by a low setting of Reynolds number, typically $0(10^{-2})$.

II. NUMERICAL ALGORITHM

A. Fundamental scheme structure

The present hybrid finite volume/element method is articulated around a time-splitting semi-implicit formulation, involving two distinct aspects: a Taylor-Galerkin scheme and a pressure-correction scheme. The Taylor-Galerkin scheme is a two-step Lax-Wendroff time stepping procedure (predictor-corrector), extracted via a Taylor series expansion in time [10, 11]. The pressure-correction method accommodates the incompressibility

constraint to ensure second-order accuracy in time (see [12, 13]). A three-stage structure emerges per time-step cycle, which can be expressed in discrete form, see [1]. Galerkin spatial fe-discretisation is employed within the momentum equation in stage 1 (matrix A_u), the pressure-correction in stage 2 (stiffness matrix A_2) and the incompressibility constraint in stage 3 (mass matrix A_3).The momentum diffusive terms are treated in a semi-implicit manner to enhance stability. The resulting augmented-Galerkin Mass matrix-vector equations at stages 1 and 3 are solved using an efficient element-by-element Jacobi scheme. The required levels of convergence are attained with only a handful of such Jacobi iterations. A direct Choleski decomposition procedure is invoked to handle stage 2.

It is the discretisation of stress that dictates the nature of the implementation. For a pure fe method, stress matrix, A_τ, is sparse and of Galerkin form. In contrast, for the hybrid finite volume/element scheme, represented as fv, A_τ is taken as the identity matrix. Hence, the need to resolve a matrix-vector equation is avoided, and the right-hand side vector b_u is straightforward to construct. Spatial discretisation is based upon six-noded fe-triangular cells, with three vertices and three mid-side nodes. Velocity and pressure interpolation is identical for either fe or fv implementation. Velocity components are computed via quadratic shape functions, using the six nodal values of the fe-triangle. Pressure is formed from linear functions, based upon the vertices alone (see Fig. 1a). Stress interpolation is of quadratic form for fe and linear for fv (with non-recovered stress gradient). With the hybrid scheme, interpolation errors may be avoided when recovering the stress nodal values for the momentum equation. This is achieved via the finite volume tessellation, constructed from the finite element grid by connecting the mid-side nodes. Four triangular fv sub-cells are generated per fe-parent triangle, Fig. 1a. The stresses are computed on the vertices of the fv-cells, as outlined below.

B. Finite volume discretisation, background

Cell-vertex fluctuation distribution schemes are used to split the flux (R) and source (Q) residuals to the vertices of each fv-triangle T. To this end, it is convenient to represent the stress constitutive equation in the form,

$$\frac{\partial \boldsymbol{\tau}}{\partial t} = -\nabla \cdot \mathcal{R} + \boldsymbol{Q} \tag{2.1}$$

$$\mathcal{R} = \boldsymbol{u}\boldsymbol{\tau} \tag{2.2}$$

$$\boldsymbol{Q} = \frac{1}{We}(2\frac{\mu_1}{\mu}\boldsymbol{d} - \boldsymbol{\tau}) + \boldsymbol{L}\cdot\boldsymbol{\tau} + \boldsymbol{\tau}\cdot\boldsymbol{L}^T, \tag{2.3}$$

thus, isolating the flux ($\mathcal{R}$) and source ($\boldsymbol{Q}$) terms.

The integration of Eqs.(2.1)-(2.3), for each scalar stress component τ, provides the time, flux and source residuals:

$$\int_{\Omega_l} \frac{\partial \tau}{\partial t}\, d\Omega = \int_{\Omega_T} \boldsymbol{u}\cdot\nabla\tau\, d\Omega + \int_{\Omega_l} Q\, d\Omega. \tag{2.4}$$

These can be evaluated over different control volumes, namely, the fv-triangle T (R_T, Q_T) or/and the Median-Dual-Cell associated to a given node l within the fv-cell T ($R^l_{\mathrm{MDC^T}}$, $Q^l_{\mathrm{MDC^T}}$). Median-Dual-Cell zones are unique non-overlapping regions defined per node l, an area one third of the triangular cell over which it is constructed, see Fig.

1b. A Median-Dual-Cell tessellation is equivalent to the Dirichlet tessellation/Voronoi region if the triangulation is of Delaunay form [14].

To summarize, a time consistent distributioned approach over flux and source terms (area-weighted [15, 16]), is paramount to ensure high-order accuracy at steady-state, and a consistent Median-Dual-Cell contribution is required to retain stability of convergence in complex flows. A generalised complete nodal update equation corresponds to the sum of contributions from all triangles surrounding node l, given by:

$$\frac{\tau_l^{n+1}-\tau_l^n}{\Delta t} = \underbrace{\frac{\sum_{\forall T}\delta_T\alpha_l^T(R_T+\beta_1 Q_T)}{\hat{\Omega}_{FD}}}_{\text{Fluctuation distribution}} + \underbrace{\frac{\sum_{\forall T}\delta_{\rm MDC}(\beta_2 R^l_{\rm MDC^T}+Q^l_{\rm MDC^T})}{\hat{\Omega}_l}}_{\text{Median-Dual-Cell}}, \quad (2.5)$$

where $\sum_{\forall T}$ represents all fv-cells surrounding node l; α_l^T the fluctuation distribution coefficients; $\hat{\Omega}_{FD}=\sum_{\forall T}\delta_T\alpha_l^T\Omega_T$, with Ω_T area for triangle T; and $\hat{\Omega}_l=\frac{1}{3}\sum_{\forall T}\Omega_T$, Median-Dual-Cell zone about node l. This approach, henceforth referred to as CT_2, has led to significant gains in accuracy and stability for steady 4:1 contraction benchmark flows [2]. Parameters $\delta_{\rm T}$ and $\delta_{\rm MDC}$ dictate different scheme options, as do boolean factor, β_1, β_2, generally taken as unity. If $\delta_{\rm MDC}=0$, MDC-forms are discarded and pure-FD schemes emerge, capable of second-order steady-state accuracy for 1D and 2D extensional flows [17]. If $\delta_{\rm T}=\delta_{\rm MDC}=1$ and $\beta_1=\beta_2$=0, a standard [R_T-FD , Q_{MDC}] fv-scheme is classified, of uniform type if $\alpha_l^T=\frac{1}{3}$ and inconsistent in control volume per term. For flows with shear, stability demands MDC-forms, $\delta_{\rm MDC}\neq 0$ with $\beta_1=\beta_2$=1. As such in Ref [1], the authors retained $\delta_T=\kappa$, with $\kappa=\xi/3$ if $|\xi|\leq 3$ and 1 otherwise, and $\delta_{\rm MDC}=1$ (see below for CT_3, with $\delta_{\rm MDC}=1-\delta_{\rm T}$). Here, $\xi=We(a/h)$, with a the magnitude of the advection velocity per fv-cell and h the square-root of the area of the fv-cell in question. A less generalised form of Eq. (2.5), inconsistent in area-weighting, would equate $\hat{\Omega}_{FD}=\hat{\Omega}_l$.

III. FLUCTUATION DISTRIBUTION SCHEMES - CHOICE OF $\boldsymbol{\alpha_L^T}$

The finite volume method presented in this paper is based on Fluctuation Distribution (FD) schemes. These are compact-stencil upwinding schemes, that update the solution in a triangular cell, by splitting flux variations to its vertices according to a prescribed strategy. Such schemes can possess properties of conservation, positivity and linearity preservation. Non-linear FD schemes can be both positive and linearity preserving, whereas linear schemes may possess only one such property.

An important aspect of fluctuation distribution is the distinction between triangles with two or one inflow side(s). This is achieved via the sign of the coefficients $k_l=\frac{1}{2}\boldsymbol{a}\cdot\boldsymbol{n}_l, l=1,2,3$, where $\boldsymbol{a}$ is the average velocity in the triangular cell and $\boldsymbol{n}_l$ the scaled inward normal to the edge *opposite* vertex l; $k_l>0$ indicates an inflow edge, that is a contribution is sent to node l, whilst $k_l<0$ designates an outflow edge, i.e. vertex l receives no contribution. Hence, triangles with two inflow sides possess two positive k_l ($k_j>0$, $k_k>0$ leading to ($\alpha_i=0$, α_j, α_k)), whereas triangles with one inflow side have one positive k_l only ($k_j>0$, so that ($\alpha_i=0$, $\alpha_j=1$, $\alpha_k=0$)). If the one inflow side situation was to prevail throughout the whole domain, all FD-schemes would collapse to the same form, thus making it impossible to conduct a comparative study.

We proceed to discuss briefly the various fluctuation distribution schemes contrasted in this study, namely two linear schemes (LDB and Lax-Wendroff) and two non-linear versions (PSI and Fluctuation Redistribution). It is important to note that fluctuation distribution schemes have been developed within the realm of pure advection equations. For more details on the theory and the construction of such upwinding schemes, the reader is referred to the work of Jameson et al. [18], Morton et al. [19], Deconinck et al. [15] and Hubbard et al. [20].

A. LDB scheme

The Low Diffusion B (LDB) scheme is a *linear* scheme. It is linearity preserving, and lacks positivity accordingly. However, it displays a relatively small amount of numerical diffusion in comparison to a linear positive scheme. The LDB distribution coefficients α_l^T are defined per cell node l according to the angles γ_1 and γ_2 in the triangle T, see Ref [1], subtended on both sides of the cell advection velocity $\boldsymbol{a}$ (an averaged velocity-vector per cell), independent of $|\boldsymbol{a}|$. The closer the advection velocity is to any given side, the more contribution is sent to the downstream vertex of that side. Our previous work on steady-state problems has proven the efficiency of LDB schemes in dealing with model problems, as well as some complex flows [1, 4].

B. Lax-Wendroff scheme

The Lax-Wendroff scheme (LW) is a *linear* (linearity preserving) scheme. It is spatially centred and second-order accurate in space. In addition, it contains a dissipation term designed to control oscillations in the neighbourhood of discontinuities, thus conferring second-order accuracy in time. Lax distribution coefficients are,

$$\alpha_l^T \ = 1/3 + \frac{\Delta t}{4\Omega_T}\boldsymbol{a}\cdot\boldsymbol{n_l^T} \tag{3.1}$$

where Δt is a time-step and $\boldsymbol{n_l^T}$ is the scaled inward-normal to the edge of triangle T, opposite to node l.

C. PSI scheme

The Positive Streamwise Invariant (PSI) scheme is a *non-linear* scheme, based on the notion of enforcing invariance along a preferred direction within a triangle. It is both positive and linearity preserving. By design, it is first-order accurate in time, and second order-accurate at steady state. The PSI-scheme is based on the so-called Narrow (N) scheme which exhibits the lowest cross-diffusion noise among linear positive schemes. To this, a MinMod limiter ($L(x,y)$) has been appended. The triangle $[\tau_i,\tau_j,\tau_k]$-solution update reads,

$$\tau_i^{n+1} = \tau_i^n + \frac{\Delta t}{\Omega_T}R_i^*, \tau_j^{n+1} = \tau_i^n + \frac{\Delta t}{\Omega_T}R_j^*, \tau_k^{n+1} = \tau_k^n, \tag{3.2}$$

$$\begin{aligned} R_i^* &= R_i - L(R_i,-R_j), R_i = -\frac{1}{2}\boldsymbol{a}\cdot\boldsymbol{n_i^T}(\tau_i^n - \tau_k^n),\\ R_j^* &= R_j - L(R_j,-R_i), R_j = -\frac{1}{2}\boldsymbol{a}\cdot\boldsymbol{n_j^T}(\tau_j^n - \tau_k^n),\\ L(x,y) &= \frac{1}{2}[1+sgn(xy)] * \frac{1}{2}[sgn(x)+sgn(y)] * min[|x|,|y|]. \end{aligned} \tag{3.3}$$

The shock-capturing capabilities of this scheme make it particularly attractive for pure advection flows. Nevertheless, it is our experience that positivity should be handled with care when source terms are involved.

D. Fluctuation redistribution scheme

The fluctuation redistribution (FR) scheme combines a low order (LO) monotone scheme (here, PSI) and a high order (HO) non-monotone scheme (here, second-order Lax-Wendroff) in such a fashion that, see Hubbard [20]: (a) the monotone scheme is favoured in regions where the solution gradient is locally high, *thus reducing the appearance of oscillations in the solution*; (b) the high-order scheme dominates in smooth flow regions to capture second-order accuracy. This combination is realised through a fluctuation **redistribution** step (akin to a predictor-corrector), whereby a nodal-limiter $[(\beta_i^T)^{max}]$ is applied to the difference between the contributions of the two underlying schemes, low-order (*LEC-PSI*) and high-order (*HEC-Lax*). Such a difference is termed an *antidiffusive cell contribution*(AEC_i^T), see [20] for details. The four phases of implementation $\forall$ node i and FV cell T are:

(i) Compute LEC_i^T; HEC_i^T; $AEC_i^T = HEC_i^T - LEC_i^T$;

(ii) $\tau_i^L = \tau_i^n + \sum_{T_i} LEC_i^T$;

(iii) Compute nodal limiter $(\beta_i^T)^{max}$; correct $AEC_i^T := (\beta_i^T)^{max} * AEC_i^T$;

(iv) final solution update $\tau_i^{n+1} = \tau_i^n + \sum_{T_i} AEC_i^T$.

IV. FINITE VOLUME DISCRETISATION, TRANSIENT CONSIDERATIONS

The above nodal-update strategies described in II. section B. have been designed with steady-state solutions in mind. In this section, we shift the focus to capturing accuracy in the transient evolution of the solution. First, we explore an optimal combination of parameters δ_{MDC} and δ_T of CT_2 (spatial weighting). Then, we consider the viability of treating the left-hand side of Eq. (2.5) in a finite element fashion, that is using a mass-matrix iteration alternative, in place of the finite volume mass-lumping approach.

A. Dynamic correction

As pointed out in section B., a Median-Dual-Cell contribution is required to ensure stability of convergence in complex flows. However, adding these contributions in an indiscriminate fashion ($\delta_T = \kappa$, $\delta_{\mathrm{MDC}} = 1$), as in Eq. (2.5), may produce additional contributions to the evolving transient solution. By design, the same should vanish once a steady-state is reached. The dependence of the parameter δ_T on the cell average-velocity, for a given We, provides an elegant way to locally adjust the contributions of the two terms of the right-hand side of CT_2 (Eq. (2.5)). Indeed, in extreme cases, δ_T would equate to 1 in fast-flow regions (usually located away from fixed boundaries), whereas δ_T would vanish on fixed boundaries (assuming no-slip boundary conditions). Hence, a natural and consistent combination choice would be (δ_T, $\delta_{\mathrm{MDC}} = 1 - \delta_T$). This would ensure a minimal Median-Dual-Cell contribution in core-flow, whilst little upwinding is imposed near fixed boundaries.

B. Consistent Mass-Matrix iteration

Commencing with integral terms from the stress equation for a fv-cell T, of area Ω_T, and Median-Dual-Cell, $\hat{\Omega}_l^T$, we observe for the right-hand-side residual, $\mathcal{L}_{rhs}(\tau)$, and three independent linear interpolation functions on the cell $\psi_i(\boldsymbol{x}), i = 1, 2, 3$, that the Galerkin terms are:

$$\int_{\Omega_T} \psi_i(\boldsymbol{x})\, \mathcal{L}_{rhs}(\tau)\, d\Omega_T, \qquad i = 1, 2, 3. \tag{4.1}$$

By taking the sum of all three contributions from the fv-cell T, this leads to

$$\sum_{i=1}^{3} \int_{\Omega_T} \psi_i(\boldsymbol{x})\, \mathcal{L}_{rhs}(\tau)\, d\Omega = \int_{\Omega_T} \left(\sum_{i=1}^{3} \psi_i(\boldsymbol{x}) \right) \mathcal{L}_{rhs}(\tau)\, d\Omega = \int_{\Omega_T} \mathcal{L}_{rhs}(\tau)\, d\Omega. \tag{4.2}$$

In other words, we extract the fv-cell contribution, having discarded the variational weighting. From this position, having gathered a single contribution to an fv-cell, one then has to construct a distribution of this quantity to the nodes of that cell. This is achieved either via "fluctuation distribution" philosophy or the "Median-Dual-Cell" construct. Within the fe-approach, the weighting deals with such matters. One may observe, in addition, that under summation of weighting functions over Ω_T, the same conclusions arise for Petrov-Galerkin weighting, irrespective of interpolation function order, that is

$$\sum_{i=1}^{i=3} (1 + \alpha_h\, \boldsymbol{u} \cdot \nabla) \psi_i(\boldsymbol{x}) = 1$$

In similar fashion, we may address the time terms, with a goal of recognising the relationship between fv and fe discretisations. Here, we may start with

$$\int_{\Omega_T} \psi_i(\boldsymbol{x})\, \psi_j(\boldsymbol{x})\, \frac{[\tau^{n+1} - \tau^n]_j}{\Delta t}\, d\Omega_T, \tag{4.3}$$

as a realisation of the Galerkin form of $\int_{\Omega_T} \omega_i(\boldsymbol{x})\, \frac{\partial \tau}{\partial t}\, d\Omega_T$, subsuming temporal gradient approximation and linear interpolation. We may express this term, via the "consistent mass-matrix" in the form,

$$\frac{1}{\Delta t}\, [M^T_{fel}]_{ij}\ \left[\Delta \tau^{n+1}\right]_j, M^T_{fel} = \frac{\Omega_T}{12} \begin{bmatrix} 2 & 1 & 1 \\ 1 & 2 & 1 \\ 1 & 1 & 2 \end{bmatrix}. \tag{4.4}$$

Equivalently, under fv weighting, $\sum_i \psi_i(\boldsymbol{x}) \equiv 1$, we would have

$$\frac{1}{\Delta t}\, [M^T_{fvl}]_{ij}\ \left[\Delta \tau^{n+1}\right]_j, M^T_{fvl} = \frac{\Omega_T}{3} \begin{bmatrix} 1 & 1 & 1 \\ 1 & 1 & 1 \\ 1 & 1 & 1 \end{bmatrix}. \tag{4.5}$$

In either fe or fv form, nodal updates are enforced through assembling the system of equations $\forall \Omega_T$. This is performed via inversion of the mass-matrix, through an efficient element-by-element Jacobi iteration. This same procedure is employed for velocity (and stress in the case of a pure fe-scheme): it is applied to nodal vector iterate $\boldsymbol{X}^{(r)}$, and appeals to a diagonalised "iterative pre-conditioner", M_d and an acceleration parameter ω. Thus, for the generalised system and over schemes of discretisation (fe or fv),

$M_{sch}\,\boldsymbol{X} = b_{sch}$,

$$M_d\,\boldsymbol{X}^{(r+1)} = (M_d - \omega\, M_{sch})\,\boldsymbol{X}^{(r)} \;+\; \omega\, b_{sch}, \qquad r = 0, 1, \cdots \tag{4.6}$$

with solution $\boldsymbol{X} = \left[\tau^{n+1} - \tau^{n}\right]$.

Here, we observe from the background theory [12, 16, 21], that element-cell contributions may be assembled, via element boolean transformation matrices L_e,

$$M_{sch} = \sum_e L_e\, M^e_{sch}\, L^T_e$$

and likewise for M_d, so that, relevant eigenvalue bounds may be established for the iteration from the element-matrix contributions. This leads to optimal acceleration parameter settings. Note, one can recover the conventional Median-Dual-Cell implementation of time, by choosing the "straight diagonal" $(M_d)_{fvl}$ as "iterative pre-conditioner". In this scenario, $\Omega_T/3 = \hat{\Omega}^T_l$, and the base iterate, $\boldsymbol{X}^{(1)}$ is identical to the standard MDC-treatment of the time-term, with $\boldsymbol{X}^{(0)} \equiv 0$ by default. Pursuing the iteration further (with M_{fvl} and $\omega = 1$), provides an iteration that will diverge if projected eigenvalue bounds are attained (lower bound 0, upper bound 3). This, indeed, we observe in practice. Of course, it is fairly obvious, even at the element level, that M_{fvl} is likely to lead to a non-diagonally dominant and singular system, once one considers the rhs-vector and note that nodal contributions will differ for the cell under any practical fv discretisation. Nevertheless, interpreting the fv-system in this manner, does provide us with fresh insight as to scheme choices that converge (actually work), and a point of cross-reference with other approaches.

Conversely, considering the fe-alternative, we observe that the "row-sum diagonal" choice, yields

$$(M_d)_{fel} = \frac{\Omega_T}{12}\begin{bmatrix} 4 & 0 & 0 \\ 0 & 4 & 0 \\ 0 & 0 & 4 \end{bmatrix} = \frac{\Omega_T}{3}\begin{bmatrix} 1 & 0 & 0 \\ 0 & 1 & 0 \\ 0 & 0 & 1 \end{bmatrix}. \tag{4.7}$$

So again, the base iterate, $\boldsymbol{X}^{(1)}$, provides the conventional Median-Dual-Cell fv-time representation. Such a single iteration, with absolute-value row-sum diagonalisation is often referred to in the literature as "mass-lumping" [11, 12]. However, and in contrast to M_{fvl}, one can now proceed with further iterations, due to the favourable conditioning of M_{fel}. Such time-discretisation is anticipated to improve the time-accuracy of the proposed fv-rhs-discretisation, as observed in the fe-context [10, 12].

Within the above framework, adopting M_{fel}, we have options posed as to choice of b_{sch}. Directly from fv-discretisation, we extract b_{fv} and the class of all such rhs terms. In addition, we may also call upon b_{fel}, over fv-cells, as sub-cells of parent velocity fe-cells. This may, or may not, draw upon the further complication of Petrov-, as opposed to Galerkin weighting, for the stress equation (the relevant upwinding strategy). Hybrid implementations are also clearly within our grasp.

C. Consistent fv-time scheme

From our earlier studies, we have established an effective area-weighted nodal update scheme, CT_2, incorporating both FD and MDC contributions, see Eq. (2.5). Nevertheless, this scheme only accommodates MDC-discretisation of the time term to the lhs of the equation. Noting the role of blending parameters δ_T on FD and δ_{MDC} on MDC

contributions, so that we adopt $\delta_{\rm MDC} = 1 - \delta_T$ for consistency, we may analyse each area contribution separately, for triangle T and the associated MDC for node l, deriving CT_3-scheme. This would lead to separate nodal update equations per cell, typically,

$$\frac{\Omega_T}{3}\,\frac{\alpha_l^T}{\Delta t}\,[\Delta\tau_i + \Delta\tau_j + \Delta\tau_k]^{n+1} = \alpha_l^T(R_T + Q_T), \qquad \text{on } \Omega_T,\ l = 1, 2 \text{ or } 3 \quad (4.8)$$

$$\frac{\hat{\Omega}_l^T}{\Delta t}\,\left[\Delta\tau^{n+1}\right]_l = (R_{\rm MDC} + Q_{\rm MDC})^l = b_l^{\rm MDC}, \qquad \text{on MDC.} \quad (4.9)$$

To extract a unique equation on Ω_T for node l from Eq. (4.8), demands a step, such as mass-lumping, from which,

$$\frac{\Omega_T}{\Delta t}\,\alpha_l^T\,\left[\Delta\tau^{n+1}\right]_l = \alpha_l^T(R_T + Q_T) = \alpha_l^T b^T, \qquad \text{on } \Omega_T. \quad (4.10)$$

Blending equation (4.9) and (4.10) with parameters δ_T and $\delta_{\rm MDC}$, so that $\hat{\Omega}_l^{blend} = \left[\sum_{T_l}\delta_T\alpha_l^T\Omega_T + \sum_{\rm MDC_l}\delta_{\rm MDC}^T\hat{\Omega}_l^T\right]$ and summing over cells yields scheme CT_3,

$$\frac{\Delta\tau_l^{n+1}}{\Delta t} = \frac{\sum_{\forall T_l}\delta_T\alpha_l^T b^T}{\hat{\Omega}_l^{blend_1}} + \frac{\sum_{\forall MDC_l}\delta_{\rm MDC}^T b_l^{\rm MDC}}{\hat{\Omega}_l^{blend_2}}, \quad (4.11)$$

an alternative complete nodal update to equation (2.5), with $\hat{\Omega}_l^{blend_1} = \hat{\Omega}_l^{blend_2} = \hat{\Omega}_l^{blend}$. From this adjusted form, we observe that a uniform distribution α-scheme ($\alpha_i^T = 1/3, \forall i, T$) on time terms would generate an area factor of $\hat{\Omega}_l$. One notes the versatility of CT_3, if $\hat{\Omega}_l^{blend_1} = \hat{\Omega}_{FD}$ and $\hat{\Omega}_l^{blend_2} = \hat{\Omega}_l$ regenerating Eq. (2.5). In the more general state, the blending parameters themselves direct the precise composition of area-weighting, hence governed by local dictates. We proceed to demonstrate the effective nature of CT_3, in contrast to CT_2, through practical temporal implementation, noting that we may treat these variants as delivering alternative rhs-vectors b_{sch}. Consequently, consistent mass-matrix iteration may be layered upon each alternative, as required.

V. PROBLEM SPECIFICATION

To investigate the performance of the different fluctuation distribution schemes presented in section III., and the solution-update strategies discussed above (consistent FD fv-approach of Eq. (2.5) ($\delta_T = \kappa$, $\delta_{\rm MDC} = 0$), CT_2 of Eq. (2.5), CT_3 of Eq. (4.11) and mass-matrix of Eq.(4.6)), we consider planar start-up channel flow (Poiseuille flow). This is a transient problem, when initiated from rest. For the Oldroyd-B model fluid, this flow is equipped with an analytical transient solution in velocity and stress, provided by Waters and King [9]. The transient-stress exhibits both overshoots and undershoots as it evolves towards a steady-state. The problem is a pure transient shear flow computed upon an unstructured mesh, see Fig. 2. Such choice is ideal for the purpose of this study, since it is sufficiently crude to stimulate differences between various scheme implementations, but not so crude as to significantly degrade solution quality. Also, on unstructured meshes the two-inflow side condition per element is ensured, so that the various FD-upwinding schemes may be distinguished.

Following the Waters and King transient analytical solution, velocity components are imposed both at the inlet and exit, whilst stress is imposed at the inlet only. Pressure

is set at a boundary exit point to remove the indeterminacy of pressure level. No-slip boundary conditions prevail at the walls. The non-dimensional parameters are $\mu_1/\mu = 8/9$, $\mu_2/\mu = 1/9$. These ratios correspond to representative values used in the literature, when studying highly viscoelastic fluids. We start with a typical time step of order $0(10^{-2})$ and the level of $We = 1$. Here usually, five Jacobi iterations are enough to reach convergence for the fe-stages. We have recourse to different number of iterations to determine optimal settings, since iteration numbers can be different for stress and/or velocity components of the system. The time-stepping termination criteria is taken as 10^{-5}, governing a relative solution temporal increment within a least squares measure [17, 5]. All solutions are compared against the transient analytical solution, both at a boundary and at an interior node. Solution quality is judged on two criteria: keeping in phase with the analytical solution, and minimisation of the relative error to the analytical solution throughout the transient development, and steady-state. We retain Node 39 $[x = 1.2, y = 0.0]$ and Node 62 $[x = 0.62, y = 0.6]$, respectively (see Fig. 2). In this way, we are able to establish the properties of the various implementations without any boundary influence. Also, we can investigate the potential of improving the solution by specific treatment of the boundary, if so required.

VI. DISCUSSION OF RESULTS

We proceed to scrutinise our implementation results for start-up channel flow and transient response for the various fv-nodal updates discussed above, organised into sections on pure FD-schemes, hybrid schemes, MDC inclusion, and mass-matrix iteration. We focus attention entirely upon all-important stress evolution. As demonstrated in the following sections, it is necessary to segregate behaviour at the shear boundary from that in core-flow. Table I charts the number of time-steps required for each FD-scheme (without MDC, $\delta_{MDC} = 0$) to achieve steady-state, and the departure from the analytical solution at predefined instants that correspond to the successive peaks in transient stress-evolution (peaks 1-3, long-time). Table II quantifies the same when MDC is included. We refer to these tables in the discussion below. Default options, if not otherwise stated, are: CT2, $\delta_{MDC} = 1$, with LDB FD-scheme.

Pure FD-schemes, less MDC (δ_{MDC}=0): A1. Shear boundary Fig. 3a contrasts the three cell-vertex Fluctuation Distribution schemes of interest, that form the backbone for the present numerical study: LDB (linear and linearity-preserving), PSI (non-linear and positive) and Lax-Wendroff (linear, central-scheme with dissipation). Note, these FD-schemes are applied consistently to both flux and source terms. The LDB-scheme undershoots the analytical solution throughout, starting from peak-1, and gradually asymptotes towards analytical steady-state form. The PSI-scheme almost replicates the transient (analytic-form) throughout, albeit with a minor undershoot at peak-1, and a minor overshoot, thereafter. Steady-state is captured as well. The LW-scheme manifests response similar to that of LDB, but with more pronounced undershoot. A quantitative summary is provided in Table I, in terms of peak errors, taken relatively to the analytical solution. For the shear boundary, PSI raw-results are clearly superior over all three options (up to five times better, worst-case).

Pure FD-schemes, less MDC (δ_{MDC}=0): B1. Core-flow In Fig. 3b, we contrast the base FD-schemes, impinging consistently on both flux and source terms *without MDC contributions*. The LDB-scheme (linearity-preserving) reasonably captures

the analytical solution, particularly beyond peak-2 (except for an overshoot at peak-1 and undershoot at peak-2). PSI-scheme (positive) undershoots throughout, and is conspicuous in that it exhibits a constant departure from the analytical solution at long-time. Performance of the LW-scheme is ubiquitous: this scheme overshoots until peak-3, then undershoots, before converging to the steady-state analytical solution. Table I summarises the departure of these solutions from analytical form. It is clear that the various schemes do not replicate the features exhibited within shear-boundary flow. In particular, the positive PSI-scheme fails to capture long-time transients, and undershoots peak-1 in core-flow. We emphasise, that this same scheme approximated the analytical solution closely in the boundary zone, see Fig 3a. Paradoxically, the most promising FD-scheme in core flow is the LDB-scheme (particularly so, beyond peak-2 and as time advances).

Hybrid FD-schemes, less MDC (δ_{MDC}=0***): A2. Shear boundary*** Elsewhere, positive FD-schemes have been introduced for pure advection problems. Hence, we have tested various update-strategies, without applying PSI to source terms. Eq. 2.5 with δ_{MDC}=0 is segregated to allow one FD-scheme to apply to R_T, with a second acting on Q_T, e.g. [PSI(R_T),LDB(Q_T)]. In the boundary zone, none of these hybrid schemes improve upon the exceptional quality of the consistent PSI-option, as demonstrated in Fig. 4a and results of Table I. The FR-option, mimics PSI-results closely at peak-1, but thereafter adopts Lax-form. Infact, any option with Lax-inclusion, degrades from PSI, following Lax. Schemes with PSI-LDB mix, are heavily influenced by PSI (at the boundary) and prove reasonable candidates to pursue (see on for core-flow). Notation [PSI,LDB/LDB], implies average [PSI,LDB] contribution to R_T, with pure-LDB on Q_T.

Hybrid FD-schemes, less MDC (δ_{MDC}=0***): B2. Core-flow*** The combined schemes are slightly out of phase with regard to the analytical solution, as demonstrated in Fig. 4b. All suffer degradation in long-time development, as with PSI. Noticeably, the larger the LDB-contribution to the combined scheme, the closer the solution to the analytical steady-state value. Overall, the [PSI,LDB/LDB] is preferred, though cannot surpass the exceptional performance of pure-LDB after peak-2. Note, the first-peak is almost captured (within 1.7%) by any hybrid-combination attempted (attributed to PSI-influence), with the exception of the FR-results. The failure of this FR-scheme is disappointing, since its application to pure advection problems was promising for transient model flows [20].

MDC-inclusion ($\delta_{MDC}\neq 0$***): A3. Shear boundary*** For complex flows, our past experience has been that MDC-contributions are required to ensure numerical stability [1, 2]. In addition, *consistent* MDC-inclusion is paramount to reflect transient accuracy. Indeed, the $[\delta_{\rm MDC}=1, \delta_T=f(\xi)]$ combination (standard CT_2) is poor, as compared with that of other cases at peak-1 for the boundary node, almost doubling the magnitude of the analytical solution. This would indicate that a greater domination through the $\delta_{\rm MDC}$-term (with lesser from the FD-part) is required in the boundary region, since the average velocity is minimal there. In this respect, even a standard inconsistent ($\alpha R_T + Q_{MDC}$) scheme would perform reasonably well, with heavy-side weighting to source-MDC terms. Here, the *optimal combination* of $\delta_{\rm MDC}$ and δ_T is gained when $\delta_{\rm MDC} = 1-\delta_T$ (so, compatible blending functions). Indeed, for this model problem the value of h is between 0.04 and 0.06, whilst the magnitude of the advection velocity is unity at channel-centre and vanishes as one approaches the boundary. Therefore in core-flow, the value of δ_T tends to 1 and $\delta_{\rm MDC}$ to 0, since $|\xi| > 3$. Alternatively, the value of δ_T practically vanishes towards the boundary, where $\delta_{\rm MDC}$ dominates. This setting concurs well with

[1, 2] and the case $[\delta_T = 1, \delta_{\rm MDC} = f_1]$, where $f_1 = 1$ at boundary points, and $f_1 = 0$ elsewhere.

Henceforth, we pursue PSI and LDB FD-schemes further, since these two schemes outperformed others, in the absence of MDC-contributions. Commencing with LDB, Fig. 5a confirms the judicious choice of $[\delta_T, \delta_{\rm MDC}$=1-$\delta_T]$-combination for CT_2 (noting, the comment above with $\delta_{\rm MDC} = 1$). Indeed, the relative error at peak-1 is reduced impressively, from 100% to a mere 4%, see Table II. In contrast, for CT_3 in-phase results are derived, and retaining $\delta_{\rm MDC} = 1$ does not degrade the solution from $\delta_{\rm MDC} = 1 - \delta_T$. On the contrary, setting $\delta_{\rm MDC} = 1$ improves the solution marginally, above $\delta_{\rm MDC} = 1 - \delta_T$. This reflects the superior consistency in term-weighting of CT_3, upon inclusion of MDC-contributions. Consequently, we retain CT_3, henceforth. Note, the maximum relative error for the (LDB,$[\delta_T, \delta_{\rm MDC} = 1]$)-nodal update is 4% (corresponding to peak-1), which reduces to 0.3% at steady-state. Note, the PSI-scheme remains optimal at the boundary, as indicated in Fig. 5a and Table II for (PSI,$[\delta_T, \delta_{\rm MDC} = 1]$). The relative error achieves its maximum at peak-1 (2.4%), declining to 0.1% at steady-state. The option with $\delta_{\rm MDC} = 1 - \delta_T$ is marginally better at peak-2, but worse elsewhere. All such error bars are dramatically reduced with h-reduction $[\frac{1}{2}, \frac{1}{4}]$ and Δt-reduction through one and two orders (see [22]).

MDC inclusion ($\delta_{MDC} \neq 0$): B3. Core-flow Finding in core-flow, re-echoe those for near-shear-boundary flow. More specifically: using δ_{MDC}=1 with CT_2 introduced oscillations around peak-1, (instead of doubling the first-peak magnitude, as near the boundary); appealing to the δ_{MDC}=1-δ_T choice corrects for this, to produce a solution similar to that of a consistent pure-FD-approach, see Fig. 5b. Here, again, the choice of δ_{MDC} is not critical for CT_3, though the slight improvement brought about by δ_{MDC}=1 on the boundary, is marginal in core flow. Finally, as anticipated, PSI with MDC, inherits the long-time behaviour of PSI without MDC. Short-time response (peak-1,-2) are quite respectable, so that PSI-MDC displays good first-peak performance. Quantification is provided in Table II.

Here, it is worth mentioning that the axial velocity component for this 10x10 crude mesh is predicted to lie within a few percent of the transient analytical solution. The numerical solution captures the transient development at all the peaks/troughs, and long-time behaviour within 0.04% of the analytical solution. The relative error declines upon the refined 40x40 mesh, as shown in Fig. 8a,b. The sampled boundary and internal nodes of reference are [x=1.2, y=0.0] and [x=0.56, y=0.65], respectively. At this level of refinement and time-step selection of $0(10^{-4})$, the [LDB, CT3]-scheme sharply captures the transient response, throughout the transient development and onwards towards steady-state. For example, τ_{xx} maximum relative error at steady-state, on interior and boundary sample points is 0.13% and 0.049%, respectively. In this study, we have focused on the more stringent scenario of unstructured meshing, generally unavailable to spectral element schemes in the wider context. Our extensive earlier analysis, over mesh refinement and time step reduction, would point to second-order spatial accuracy and temporal accuracy between first and second order (see [22, 23]).

Mass-matrix weighting ($\delta_{MDC} \neq 0$): A4. Shear boundary We proceed to investigate the effect of introducing mass-matrix-iteration, in its treatment of the time integral, see Fig. 6a. We recall that raw CT_3-schemes are equivalent to using a single-iteration (m1). In addition, when appealing to mass-matrix iteration, iteration is avoided at boundary points, as this introduces significant accuracy degradation. Empirical estimation has revealed that two mass-iterations is optimal.

For the LDB-m2 scheme, the improvement brought about by mass-matrix iteration over pure-CT_3 is striking for the boundary solution, especially in the short-time transient. Indeed, this LDB-m2 scheme tallies closely with [CT_3-PSI]-results throughout, with the exception of a slightly more pronounced undershoot at peak-1. Relative errors for peak-2 and peak-3 are now quite respectable with LDB-m2. This is significant, since none of the strategies involving mass-lumping (m1) could compete against the pure-FD (PSI) nodal-update.

Moreover, incorporating mass-matrix iteration into [CT_3-PSI], degrades solution quality at the boundary beyond peak-1 (which itself is remarkably good), with respect to pure [CT_3-PSI], irrespective of number of iterations employed (see Fig. 5a versus Fig. 7a). The situation is similar with reduction in δ_{MDC} from unity.

Mass-matrix weighting ***($\delta_{MDC} \neq 0$): B4. Core-flow*** Under such weighting, there is positive impact upon the LDB-scheme, as was the case with boundary-flow. Now, peak-1 is captured upon iteration. This is followed by a minor overshoot around peak-3. These characteristics are judged against the significant first-peak overshoot and second-peak undershoot of LDB without mass-matrix weighting of Fig. 6b. So, iteration aids [CT3-LDB] in core and boundary flow.

In contrast, for the positive PSI-scheme in core-flow, recourse to mass-matrix-weighting does not improve long-time behaviour and departure from the analytical solution is conspicuous. It accentuates the undershoot at the first-peak, see Fig. 7b in contrast to Fig. 5b.

For LDB, a dynamic adjustment may be more appropriate here, so that gradually iteration would be phased out as time advances (say, beyond peak-2). Preliminary evidence would indicate that such a time-switch is effective, at both boundary and within core-flow, noticeably once the strength of solution-oscillation has abated to beyond peak-3. Dynamic algorithmic adjustment may of course be enforced on alternative portions of the schemes constructed. Notably, an average of (CT2/CT3)-LDB, performs well at boundary-peak1 (as [PSI,CT3,m2]).

VII. APPLICATION TO A COMPLEX FLOW

We extend the application of the optimal scheme, derived in the previous section [LDB,CT3, $\delta^T_{\mathrm{MDC}} = 1$], to start-up creeping flows within a 4:1 planar contraction (Fig. 9). Creeping flow is approximated via a low setting of Reynolds number, typically $0(10^{-2})$. We observe that solutions for Reynolds number 0, 10^{-4} and 10^{-2} are practically identical. Here, we focus upon the issue of the influence of time-dependent inlet boundary conditions settings on flow-structure, see Waters and King [9]. Transient velocity-components are imposed at inlet and exit-flow stations, and transient stress-components at the inlet station only. A pressure level may again be set at the inlet-station (or exit), and symmetry is imposed at the centreline. No-slip boundary conditions are retained on static wall boundaries. To reflect the transient nature of the solution, Fig. 10 charts the *centreline-velocity* against time, monitored at the *inlet* zone for $We = 1.0$ and $We = 2.5$. The first peak [P1], corresponds to the first overshoot at t=0.52 units, [P2] to t=1.58, [P3] to t=2.60 and the last [P4] to steady-state at t=8.8 units for $We = 1.0$. Fig. 11 demonstrates the transient evolution of velocity-vectors for the $We = 1.0$ solution, from a short-time (t=0.20 units) after start-up of flow, till the ultimate steady-state is reached (t=8.80 units). A salient-corner vortex builds-up gradually to time-P1 (first-

overshoot, t=0.52 units). As centreline-velocity gradually declines (cf. Fig. 10), a large secondary-vortex appears (half-way between P1 and P2 time). This extends way back upstream, signalling the appearance of a reverse-flow region (near the upstream-wall). As centreline-velocity rises towards P3 time(t=2.60), reverse-flow is progressively neutralised, till it disappears altogether. This occurs half-way between P2 and P3, at around t=2.60 units, where the salient-corner vortex has almost disappeared. From this point onwards, the salient-corner vortex starts to grow oncemore, before gradually decreasing towards its steady-state form.

Next, we proceed to investigate flow-structure evolution at higher levels of elasticity. The largest such level of We to be reached with such true-transient solutions was $We = 2.5$.[1] Fig. 12 charts velocity-vectors against time, from early development (the first velocity overshoot, t=0.70 units) until steady-state (t=30.0 units). The unique evolutionary flow features observed for the less-elastic fluid ($We = 1.0$) are replicated, and amplified. Here again at $We = 2.5$, transitions are dictated by the inlet-velocity peaks Q1-Q3 (annotated in Fig. 10). A salient-corner vortex becomes apparent at Q1 (t=0.70 units). The reverse-flow region that appears half-way between Q1 and Q2, now expands internally towards core-flow. This secondary-vortex reaches a maximum width at t=2.90 units, covering about half the upstream-crossflow region. Subsequently, as the centreline-velocity increases towards Q3, again there is a gradual neutralisation of back-flow, until its total disappearance at t=3.70 units, between Q2 and Q3 (t=4.10 units). From this point-onwards (Fig. 12), salient-corner vortices start to grow oncemore, and evolve towards their steady-state forms, with only minor fluctuations in their respective sizes. These dynamic fluctuations in flow-structure (increase/decrease) reflect the gradually dampened oscillations in the inlet velocity-profile, that die away as the velocity asymptotes towards its steady-state plateau-value. The stress field structure is reported via transient stress-contours in Fig. 13, for first normal stress-difference (N_1 = τ_{xx} - τ_{yy}) and shear-stress, respectively ($We = 2.5$, elastic components alone). The times reported are selected to identify the principal states of evolutionary development in passage to steady-state. One may comment that steady-state structure around the re-entrant corner is established somewhat earlier in normal-stress (by t=3.70) than shear-stress (t=10.0). This is also reflected in the more dramatic adjustment required in the salient-corner zone in shear-stress, as required to define the emerging vortex structure.

VIII. CONCLUSIONS

This paper has demonstrated the properties of some fv/fe-schemes for transient simulations of Oldroyd-B model viscoelastic flows, using a model problem with a variety of fv-constructs, and a 4:1 contraction flow. In particular, we have considered various fluctuation-distribution forms, different Median-Dual-Cell (MDC) combinations, and alternative fv-time schemes. Numerical results have been compared against a transient analytical solution and the influence of various factors has illustrated the principal issues of relevance in attaining highly-accurate solutions. Favourable scheme properties are

[1] Alternatively, with an interest in only steady-solutions, larger We-levels of 4.6 may be achieved [3] by using a pseudo-transient continuation procedure to gradually progress through lower We-solution states, see Sato and Richardson [6]. Mesh refinement studies are covered in [3].

derived, providing those, evidently capable of capturing physical oscillations accurately in the transient, whilst retaining stability.

Our prior work has revealed that for steady-state problems, consistency in combination of flux and source terms was vital to retain, second-order accuracy. Furthermore, when considering complex flows, consistent inclusion of MDC-contributions was paramount to ensure numerical stability. Results of the current study would indicate, that a judicious choice of weighting-parameters (especially those impinging on the MDC-terms) is important when considering transient evolution. A serious issue has been to extract, simultaneously, optimal numerical solutions both in core-flow and near shear-boundary flow. Paradoxically, schemes that capture transient evolution well near boundaries, fail to do so in core-flow, and vice-versa. We have been able to resolve this dilemma by introducing consistent mass-matrix weighting (mimicking fe-form) upon time-terms. In doing so, it has been necessary to avoid iteration at the shear-boundary itself, as this degrades solution quality. An optimal iteration setting is commended for core-flow.

The detailed analysis of the various update-strategies reveals *three* important points. The *first point* is related to positive schemes, exemplified via the PSI-scheme. Though nodal-updates involving PSI capture the transient development well near shear-boundaries, they fail to capture long-time evolution in core-flow. Conversely *(point-two)*, the linearity-preserving LDB-scheme performs rather well in core-flow, especially beyond peak-2 and at long-time, but undershoots the analytical solution at the boundary, before regaining the same at steady-state. These aspects are brought out rather well in the summarial point values of Table II, where the LDB-scheme with iteration, proves overall the best option, on *both boundary and interior*. Degradation of PSI on the boundary, with iteration, or δ_{MDC}=1-δ_T, is also apparent. Attempts to spatially adjust in hybrid fashion, from PSI-boundary to LDB-core, have not substantially altered this position (though dependence upon the adaptation is subtle). The dilemma of extracting a single, generalised scheme, which is optimal in both core and boundary flow, has been overcome by appealing to the consistent mass-matrix weighting of time-terms *(point-three)*. Dynamic temporal scheme adjustment may show some promise and has been dealt with above.

We have demonstrated the extended application of our optimal scheme from the model channel problem to that of a complex transient viscoelastic contraction flow. For this 4:1 contraction flow, complex features have emerged in flow-structure, notably the appearance of a large secondary-flow at early evolution-times. Such features are novel, unexposed by fixed-point steady-state driving boundary conditions (non-time varying in velocity-stress). We have illustrated that the steady-state structure, around and after the re-entrant corner is established earlier in normal-stress than shear-stress. As such, further application of the proposed methodology is encouraged, particularly with unstructured meshing and complex flows in mind.

ACKNOWLEDGMENTS

Support from TMR/EU for MA and EPSRC for HRTJ, and academic via INNFM colleagues, Professors Walters and Phillips, is gratefully acknowledged.

REFERENCES

1. P. Wapperom and M.F. Webster. Simulation for viscoelastic flow by a finite volume/element method. *Comput. Meth. Appl. Mech. Eng.*, 180:281–304, 1999.
2. M. Aboubacar and M.F. Webster. A cell-vertex finite volume/element method on triangles for abrupt contraction viscoelastic flows. *J. Non-Newtonian Fluid Mech.*, 98:83–106, 2001.
3. M. Aboubacar, H. Matallah, and M.F. Webster. Highly Elastic Solutions for Oldroyd-B and Phan-Thien/Tanner Fluids with a Finite Volume/Element Method: planar contraction flows. *J. Non-Newtonian Fluid Mech.*, 103:65–103, 2002.
4. M. Aboubacar, H. Matallah, H.R. Tamaddon-Jahromi, and M.F. Webster. Numerical prediction of extensional flows in contraction geometries: hybrid finite volume/element method. *J. Non-Newtonian Fluid Mech.*, 104:125–164, 2002.
5. H. Matallah, P. Townsend, and M.F. Webster. Recovery and stress-splitting schemes for viscoelastic flows. *J. Non-Newtonian Fluid Mech.*, 75:139–166, 1998.
6. T. Sato and S.M. Richardson. Explicit numerical simulation of time-dependent viscoelastic flow problems by a finite element/finite volume method. *J. Non-Newtonian Fluid Mech.*, 51:249–275, 1994.
7. F. Olsson. A solver for time dependent viscoelastic fluid flows. *J. Non-Newtonian Fluid Mech.*, 51:309–340, 1994.
8. N. Fieter and M.O. Deville. Time-dependent algorithms for the simulation of viscoelastic flows with spectral element methods: applications and stability. *J. Comput. Phys.*, 186:93–121, 2003.
9. N.D. Waters and M.J. King. Unsteady flow of an elastico-viscous liquid. *Rheo. Acta*, 9:345–355, 1970.
10. J. Donea. A Taylor Galerkin method for convective transport problems. *Int. J. Num. Meth. Eng.*, 20:101–119, 1984.
11. O.C. Zienkiewicz, K. Morgan, J. Peraire, M. Vandati, and R. Löhner. Finite elements for compressible gas flow and similar systems. In *7th Int. Conf. Comput. Meth. Appl. Sci. Eng.*, Versailles, France, 1985.
12. D.M. Hawken, H.R. Tamaddon-Jahromi, P. Townsend, and M.F. Webster. A Taylor-Galerkin based algorithm for viscous incompressible flow. *Int. J. Num. Meth. Fluids*, 10:327–351, 1990.
13. J. Van Kan. A second-order accurate pressure-correction scheme for viscous incompressible flow. *SIAM J. Sci. Stat. Comput.*, 7, 3:870–891, 1986.
14. N.P. Weatherill. A method for generating irregular computational grids in multiply connected planar domains. *Int. J. Num. Meth. Fluids*, 8:181–197, 1988.
15. H. Deconinck, P.L. Roe, and R. Struijs. A multi-dimensional generalization of Roe's flux difference splitter for the Euler Equations. *Comput. and Fluids*, 22:215–222, 1993.
16. A.J. Wathen. Realistic eigenvalue bounds for the Galerkin mass matrix. *IMA J. Num. Anal.*, 7:449–457, 1987.
17. P. Wapperom and M.F. Webster. A second-order hybrid finite-element/volume method for viscoelastic flows. *J. Non-Newtonian Fluid Mech.*, 79:405–431, 1998.
18. A. Jameson and D. Mavriplis. Finite volume solution of the two-dimensional Euler equations on a regular triangular mesh. *A.I.A.A*, 24:611–618, 1986.
19. K.W. Morton, P.I. Crumpton, and J.A. MacKenzie. Cell vertex methods for inviscid and viscous flows. *Comput. and Fluids*, 22:91–102, 1993.

20. M.E. Hubbard and P.L. Roe. Multidimensional upwind fluctuation distribution schemes for scalar time dependent problems. Numerical Analysis report 1/98, Department of Mathematics, University of Reading, 1998.

21. D. Ding, P. Townsend, and M.F. Webster. The Iterative Solution of Taylor-Galerkin Augmented Mass Matrix Equations. *Int. J. Num. Meth. Eng.*, 35:241–253, 1992.

22. M.F. Webster, H.R. Tamaddon-Jahromi, and M. Aboubacar. Transient viscoelastic flows in planar contractions. *Available as CSR 7-2004, Computer Reports Series, University of Wales, Swansea, Accepted for publication, J. Non-Newtonian Fluid Mech.*, 2004.

23. M. Aboubacar, T.N. Phillips, H.R. Tamaddon-Jahromi, B.A. Snigerev, and M.F. Webster. High-order finite volume methods for viscoelastic flow problem. *In press, J. Comput. Phys.*, 2004.

TABLE I. Relative errors ($\times 10^{-2}$), unstructured mesh, peaks and steady-state, various fv-schemes, $\delta_{\mathrm{MDC}} = 0$. Time-steps to steady-state N. † Optimal-boundary, ‡ Optimal-internally.

Schemes		N		peak1	peak2	peak3	long-time
Base	LDB	796	Boundary	4.62	2.51	1.86	0.43
			Interior	$3.57^{\ddagger}$	3.47	$0.93^{\ddagger}$	$0.67^{\ddagger}$
	PSI	786	Boundary	$1.43^{\dagger}$	$1.76^{\dagger}$	$0.99^{\dagger}$	$0.28^{\dagger}$
			Interior	6.25	$1.81^{\ddagger}$	6.57	5.62
	Lax	2119	Boundary	6.83	5.62	4.32	0.34
			Interior	7.33	3.33	2.57	2.03
Mixed	*Fr*	1255	Boundary	$0.06^{\dagger}$	9.08	7.22	$0.27^{\dagger}$
			Interior	6.97	$3.15^{\ddagger}$	6.80	5.67
	PSI/LDB	1004	Boundary	2.23	$1.41^{\dagger}$	$1.87^{\dagger}$	0.51
			Interior	1.78	9.63	4.98	4.75
	PSI/Lax	808	Boundary	5.21	3.39	3.00	1.15
			Interior	$0.13^{\ddagger}$	10.60	3.86	5.01
	PSI,LDB/LDB	920	Boundary	2.02	1.59	2.33	0.28
			Interior	1.33	6.10	$2.20^{\ddagger}$	$2.11^{\ddagger}$

TABLE II. Relative errors ($\times 10^{-2}$), unstructured mesh, peaks and steady-state, CT2, CT3. Time-steps to steady-state N. † Optimal-boundary, ‡ Optimal-internally.

Schemes		N		peak1	peak2	peak3	long-time
CT2	LDB, $\delta_{\mathrm{MDC}}=1$	2457	Boundary	92.21	0.87	4.77	0.18
			Interior	33.06	22.75	5.56	0.95
	LDB, $\delta_{\mathrm{MDC}}=1-\delta_T$	1022	Boundary	3.77	1.21	0.85	0.16
			Interior	4.33	7.13	0.64	$0.63^{\ddagger}$
CT3	LDB, $\delta_{\mathrm{MDC}}=1-\delta_T$	886	Boundary	4.24	2.58	1.83	0.32
			Interior	3.54	3.38	0.23	0.70
	LDB, $\delta_{\mathrm{MDC}}=1$	922	Boundary	3.85	2.29	1.80	0.25
			Interior	3.69	3.96	$0.02^{\ddagger}$	1.00
	PSI, $\delta_{\mathrm{MDC}}=1-\delta_T$	783	Boundary	5.79	0.59	0.69	0.46
			Interior	4.71	3.82	6.74	5.66
	PSI, $\delta_{\mathrm{MDC}}=1$	874	Boundary	$2.40^{\dagger}$	0.66	0.25	$0.12^{\dagger}$
			Interior	1.32	2.75	2.55	2.89
CT3, m2	LDB, $\delta_{\mathrm{MDC}}=1-\delta_T$	1109	Boundary	2.45	0.20	$0.11^{\dagger}$	0.21
			Interior	$1.20^{\ddagger}$	2.53	1.85	0.68
	LDB, $\delta_{\mathrm{MDC}}=1$	2220	Boundary	2.97	$0.12^{\dagger}$	0.97	0.35
			Interior	2.55	$0.68^{\ddagger}$	1.23	0.96

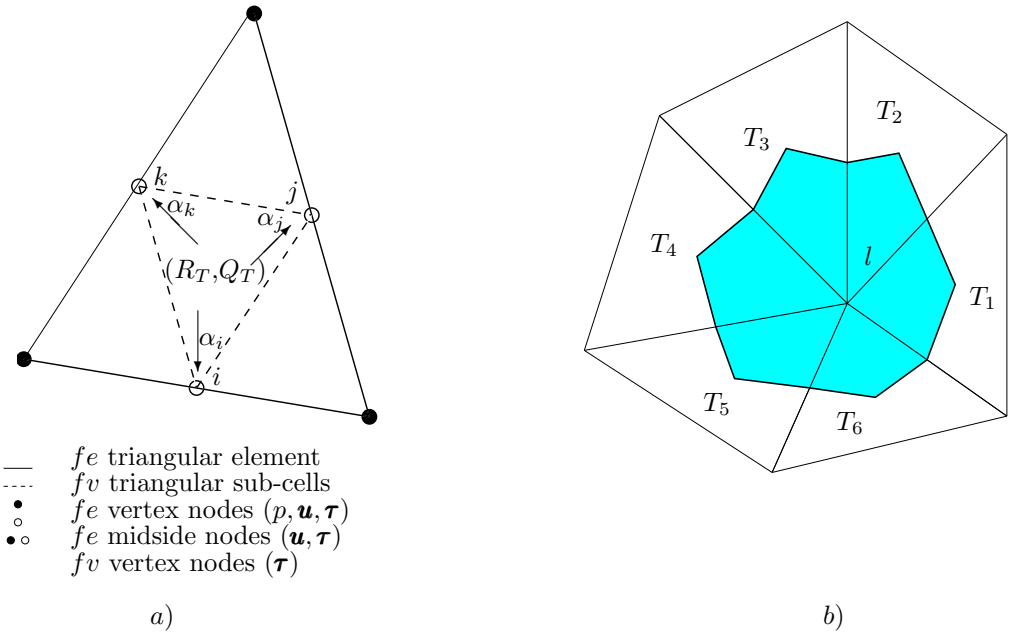

FIG. 1. Spatial discretisation, a) fe-cell with four fv sub-cells and FD per T, b) fv-control volume for node l, with Median-Dual-Cell (MDC-shaded).

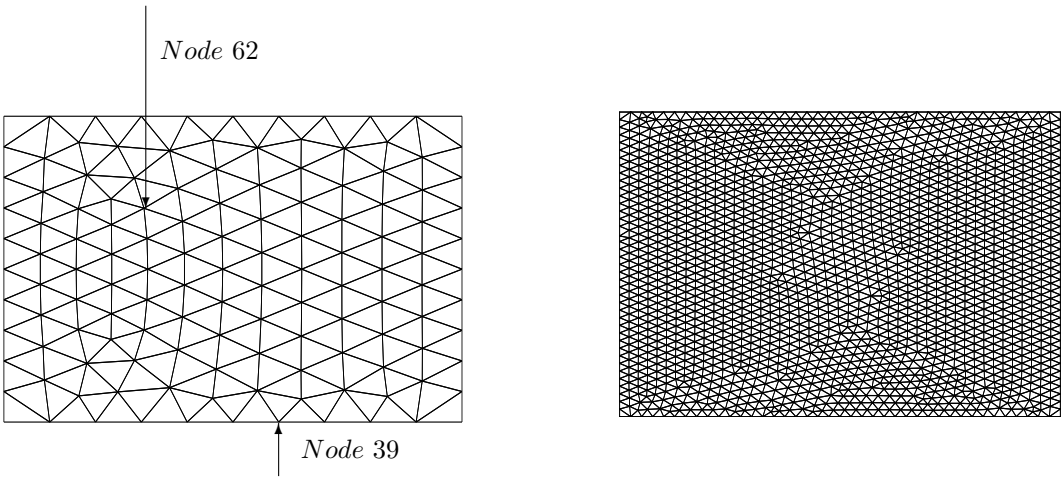

FIG. 2. Finite element 10x10 and 40x40 mesh, start-up Poiseuille flow.

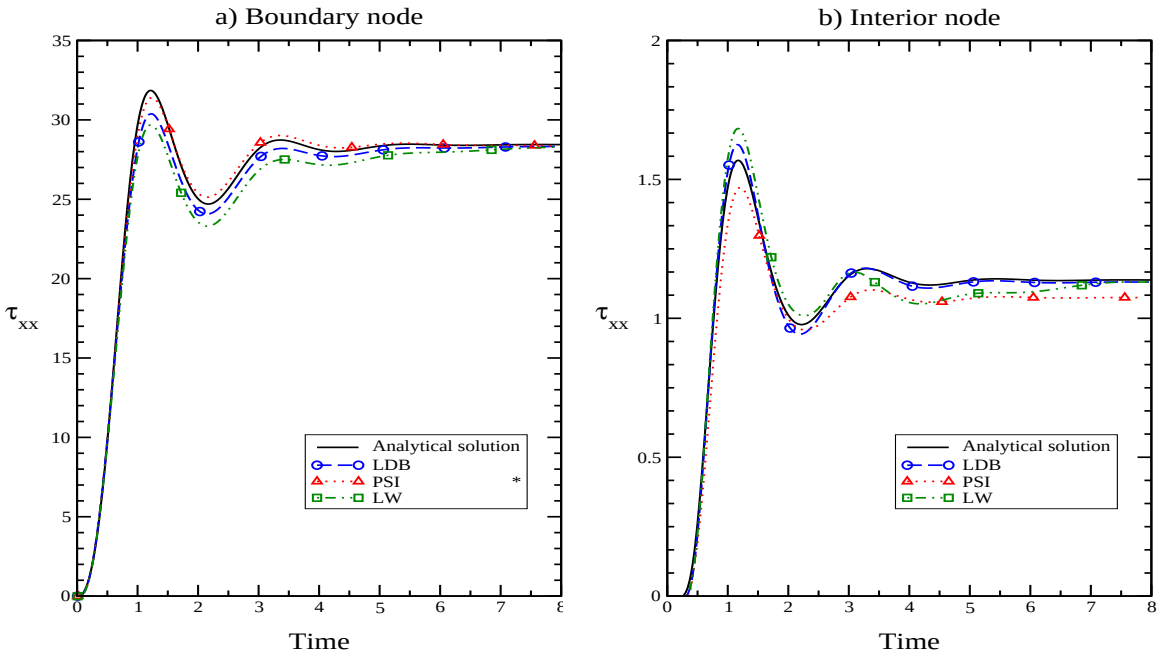

FIG. 3. a) Boundary node, b) Interior node, τ_{xx}: base FD-schemes, consistent pure-FD ($\delta_{\rm MDC}$=0), unstructured $10x10$ mesh.

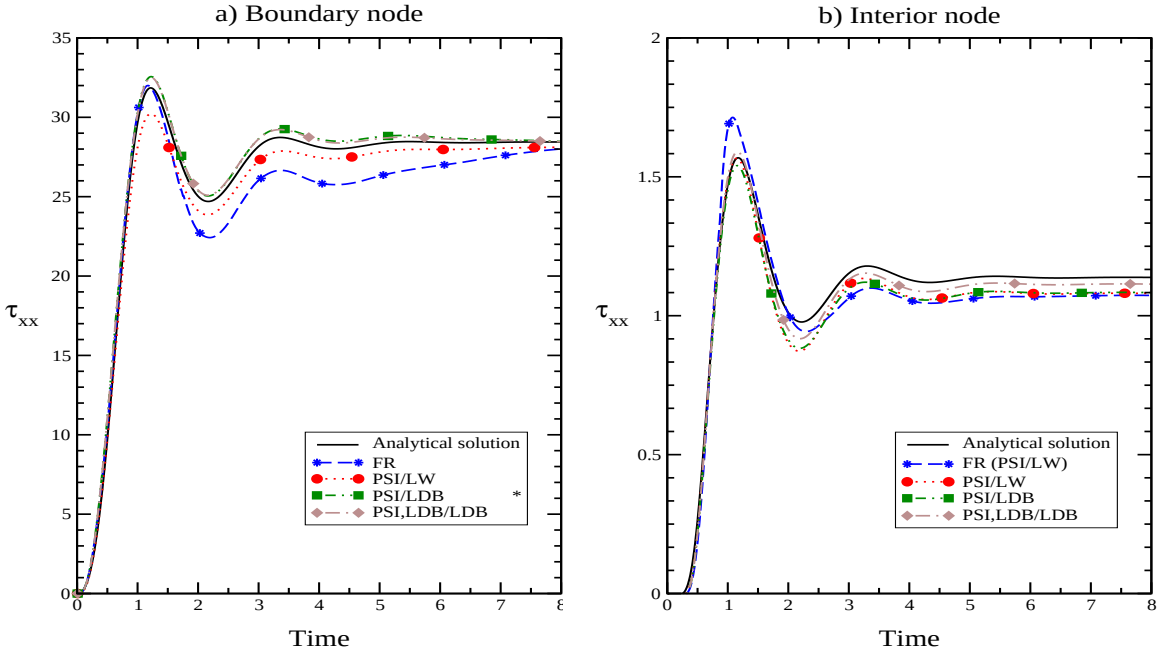

FIG. 4. a) Boundary node, τ_{xx}: hybrid FD-schemes, consistent pure-FD ($\delta_{\rm MDC}$=0), unstructured $10x10$ mesh.

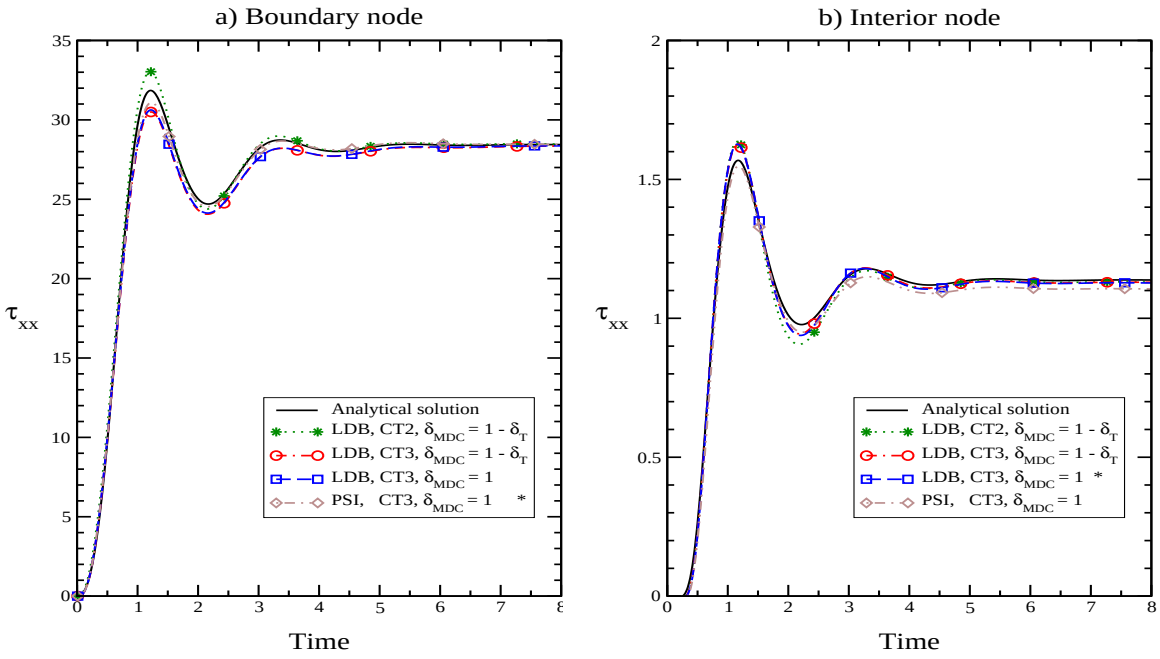

FIG. 5. a) Boundary node, b) Interior node, τ_{xx}: MDC inclusion, LDB and PSI, $CT2$ and $CT3$ various δ_{MDC}, unstructured $10x10$ mesh.

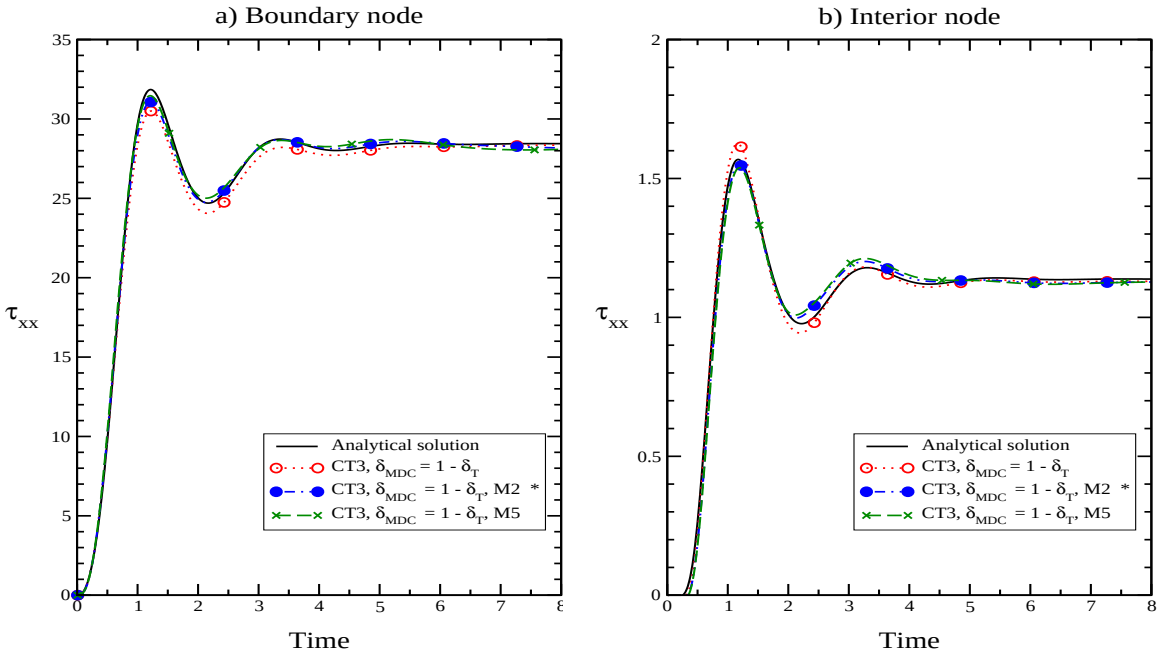

FIG. 6. a) Boundary node, b) Interior node, τ_{xx}: Mass-matrix iteration, [LDB,CT3]; 1, 2, 5 iterations, unstructured $10x10$ mesh.

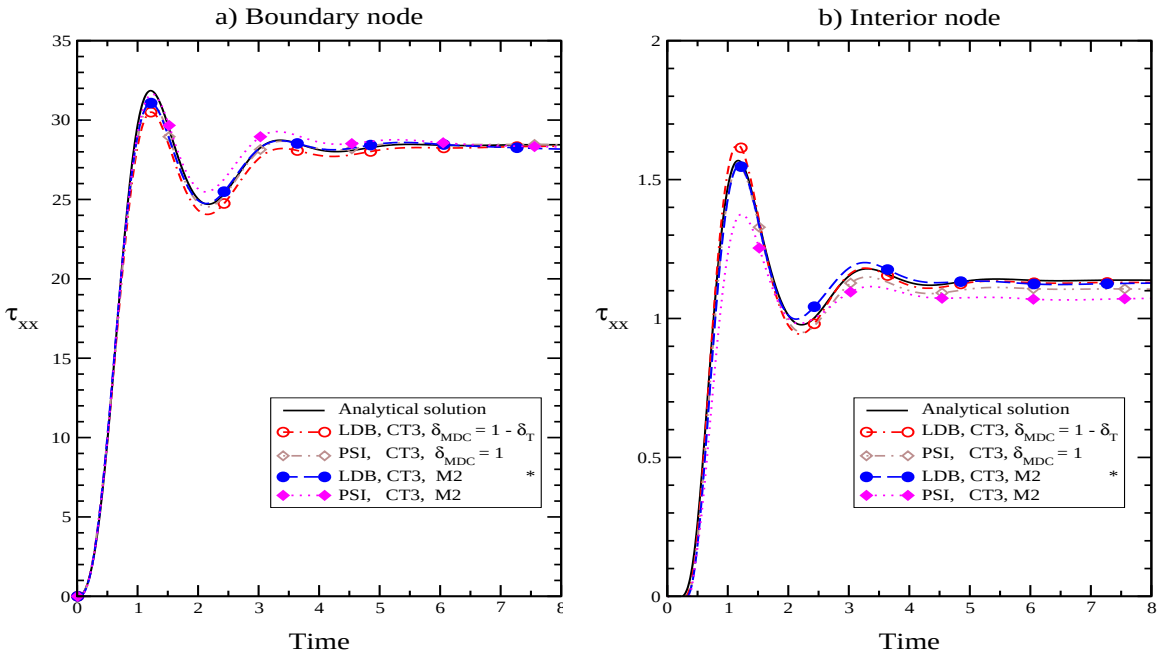

FIG. 7. a) Boundary node, b) Interior node, τ_{xx}: Optimal-combinations, PSI and LDB schemes, unstructured $10x10$ mesh.

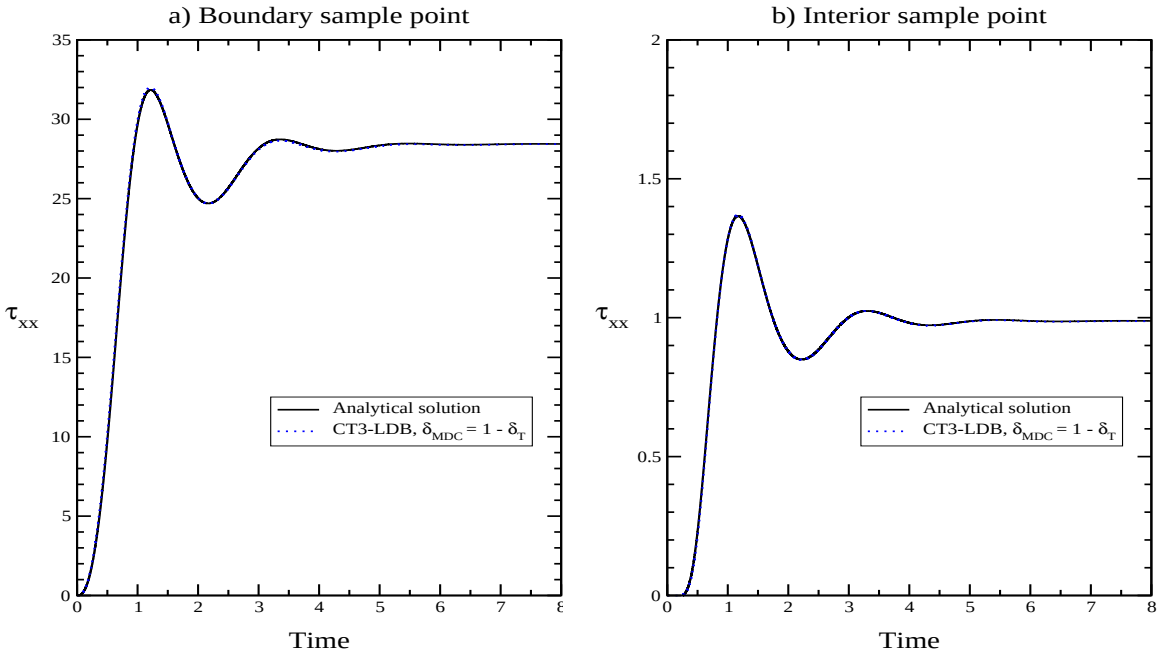

FIG. 8. a) Boundary node, b) Interior node, τ_{xx}: [CT3-LDB], start-up Poiseuille flow, refined 40x40 unstructured mesh.

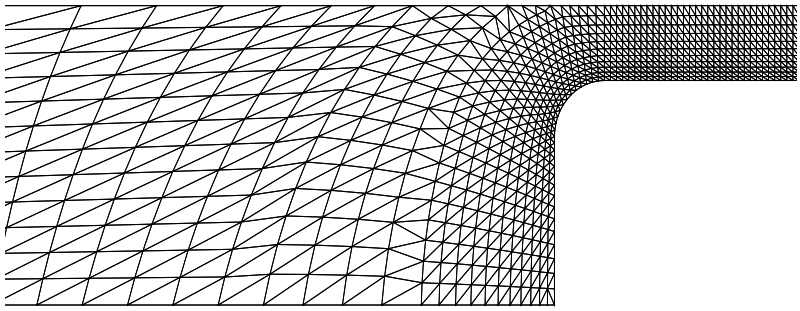

FIG.9. Planar $4:1$ *section of contraction−flow mesh*

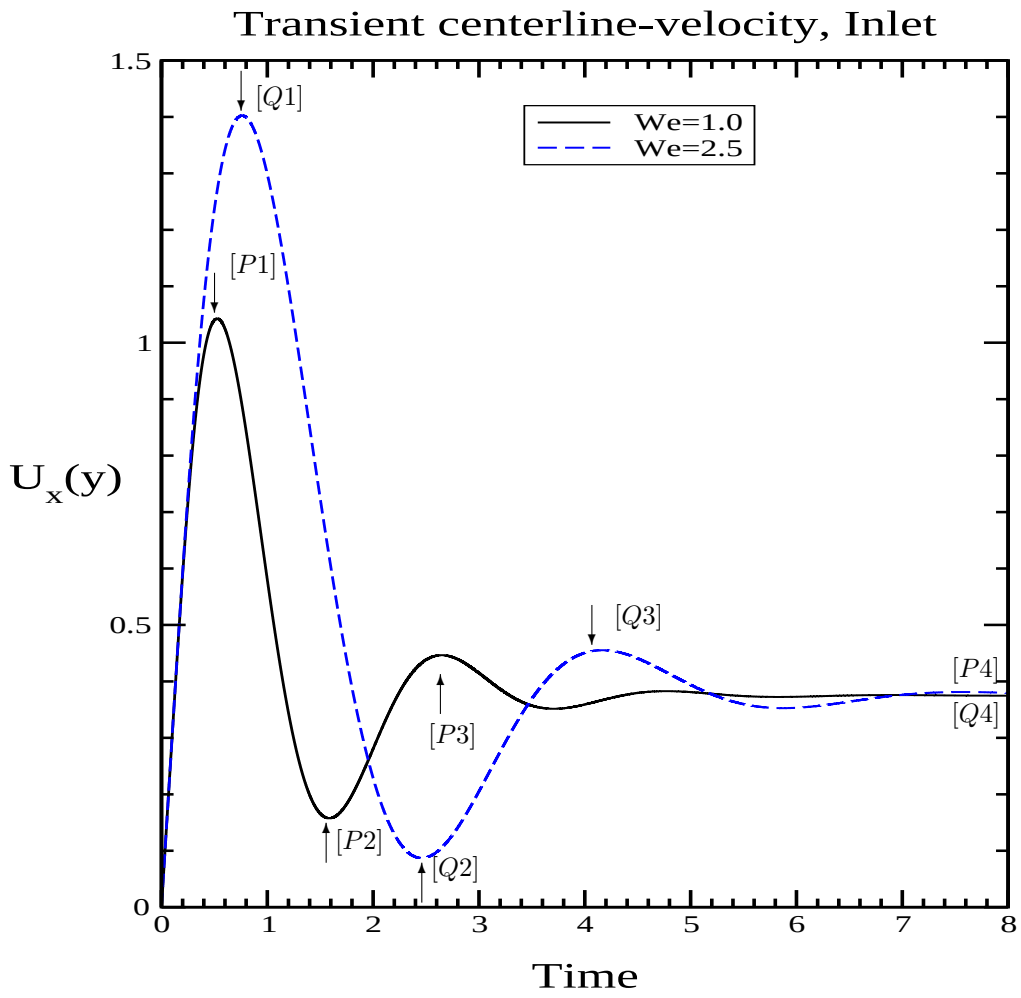

FIG. 10. 4:1 contraction, transient development of inlet centreline-velocity, [CT3-LDB,$\delta_{\mathrm{MDC}} = 1$], Oldroyd-B, $We = 1$.

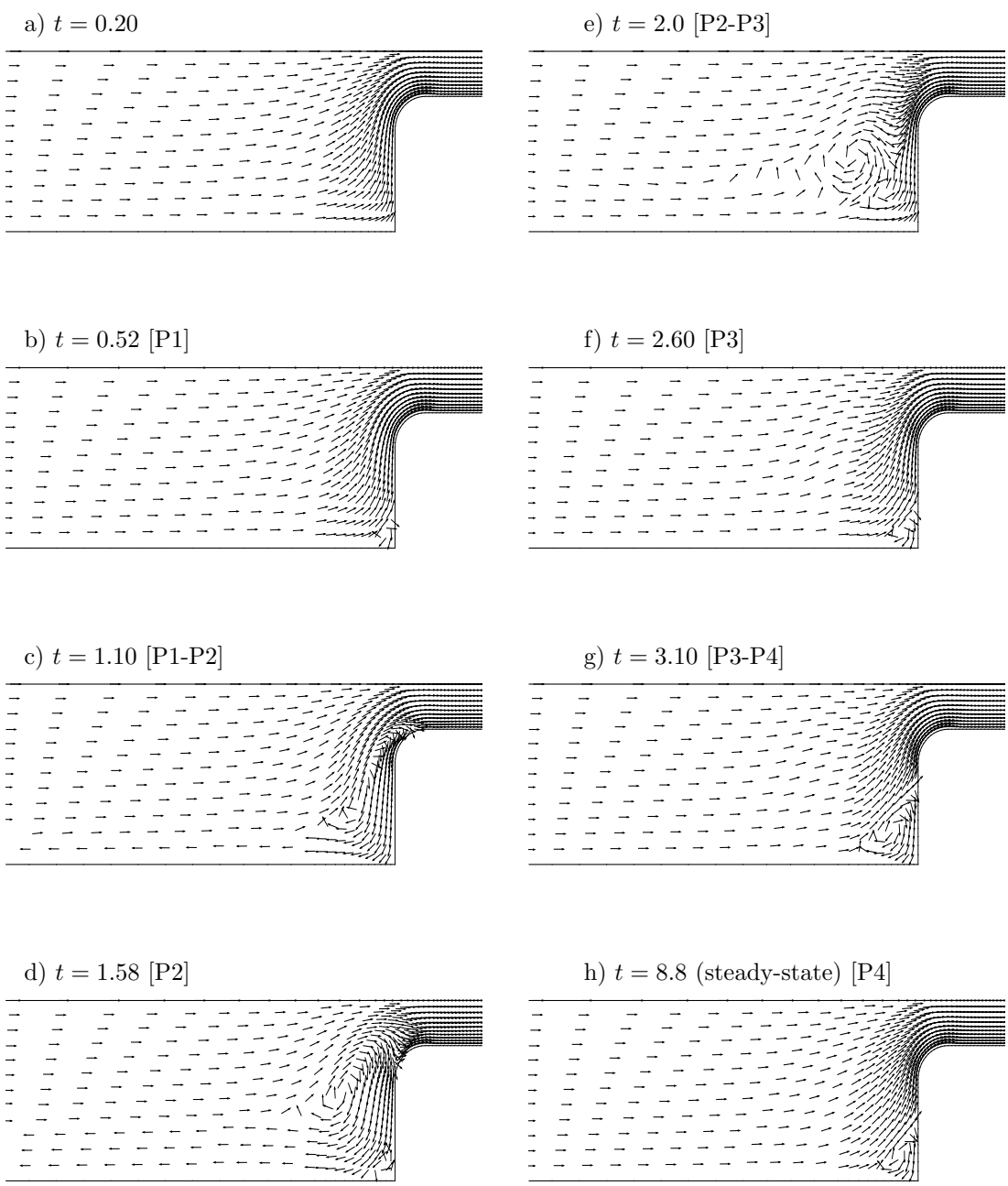

FIG. 11. Time-dependent inlet boundary conditions: transient velocity-vectors, 4:1 contraction, [CT3-LDB,$\delta_{\mathrm{MDC}} = 1$], Oldroyd-B, $We = 1$

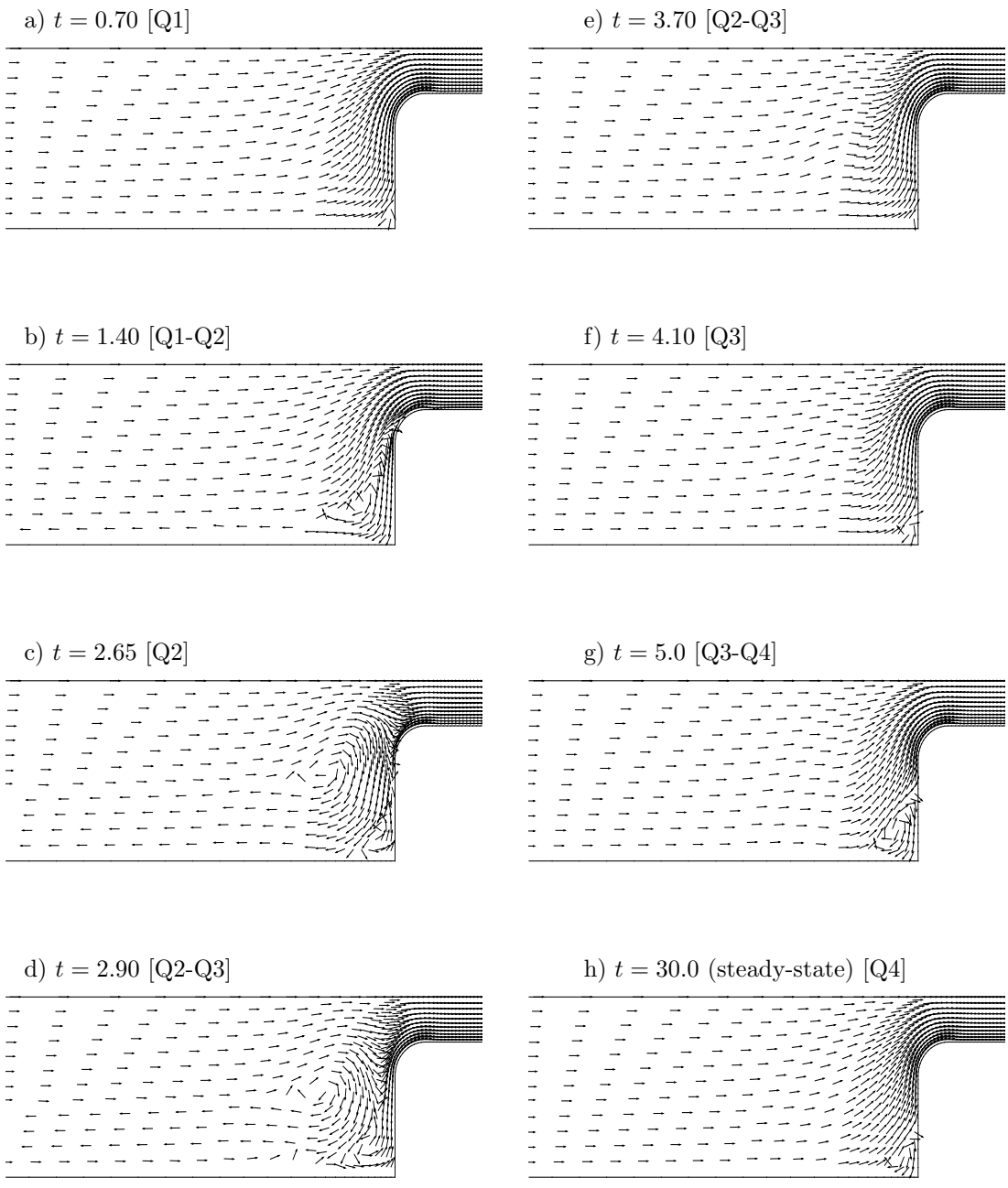

FIG. 12. Time-dependent inlet boundary conditions: transient velocity-vectors, 4:1 contraction, [CT3-LDB,$\delta_{\mathrm{MDC}} = 1$], Oldroyd-B, $We = 2.5$

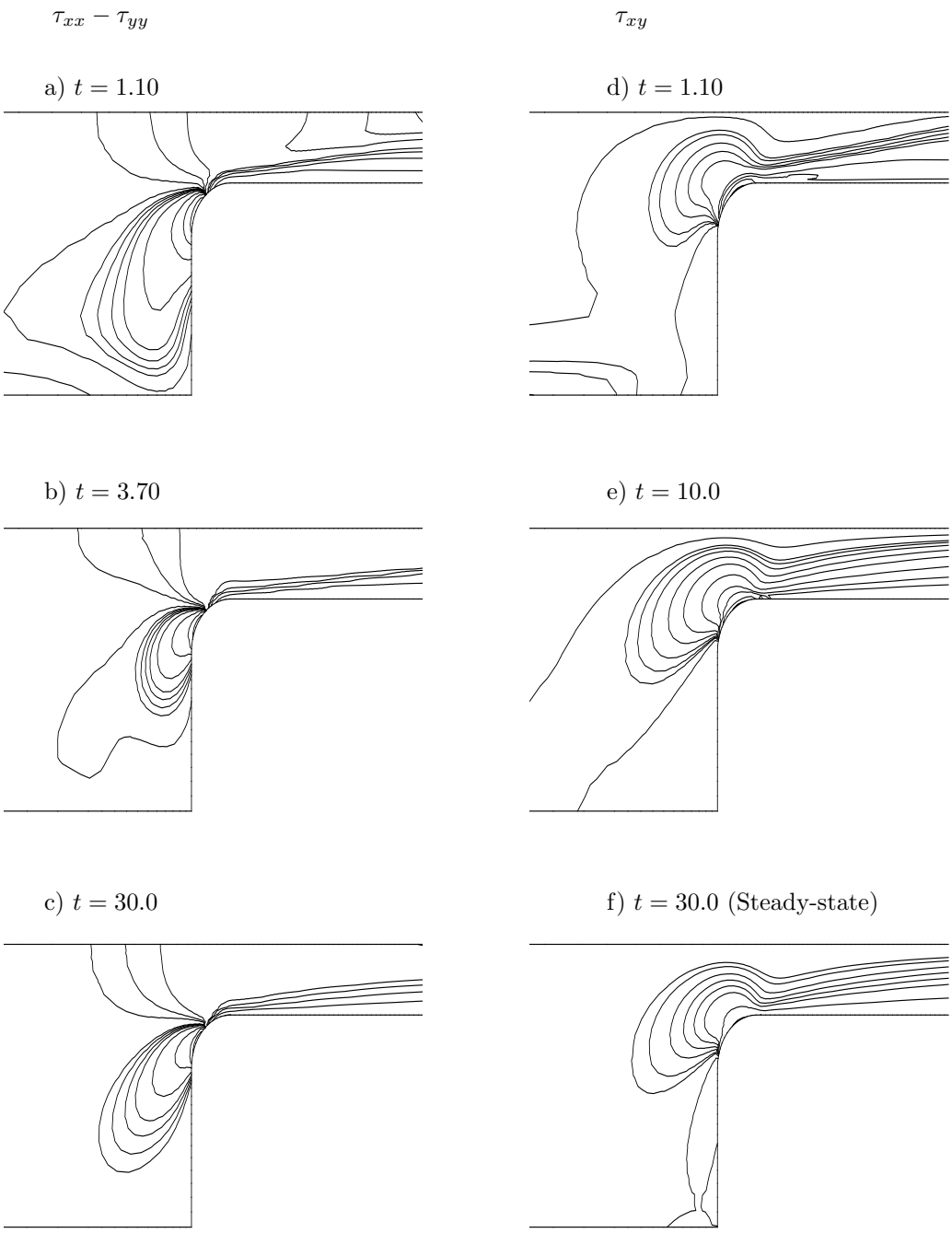

FIG. 13. Time-dependent inlet boundary conditions: transient $\tau_{xx} - \tau_{yy}$ and τ_{xy} fields, 4:1 contraction, [CT3-LDB,$\delta_{\mathrm{MDC}} = 1$], Oldroyd-B, $We = 2.5$.